

The stability of P2-layered sodium transition metal oxides in ambient atmospheres

Wenhua Zuo¹, Jimin Qiu¹, Xiangsi Liu¹, Fucheng Ren², Haodong Liu³, Huajin He¹, Chong Luo⁴, Jialin Li¹, Gregorio F. Ortiz^{1,5}, Huanan Duan⁶, Jinping Liu⁷✉, Ming-Sheng Wang⁴, Yangxing Li⁸, Riqiang Fu⁹ & Yong Yang^{1,2}✉

Air-stability is one of the most important considerations for the practical application of electrode materials in energy-harvesting/storage devices, ranging from solar cells to rechargeable batteries. The promising P2-layered sodium transition metal oxides (P2-Na_xTmO₂) often suffer from structural/chemical transformations when contacted with moist air. However, these elaborate transitions and the evaluation rules towards air-stable P2-Na_xTmO₂ have not yet been clearly elucidated. Herein, taking P2-Na_{0.67}MnO₂ and P2-Na_{0.67}Ni_{0.33}Mn_{0.67}O₂ as key examples, we unveil the comprehensive structural/chemical degradation mechanisms of P2-Na_xTmO₂ in different ambient atmospheres by using various microscopic/spectroscopic characterizations and first-principle calculations. The extent of bulk structural/chemical transformation of P2-Na_xTmO₂ is determined by the amount of extracted Na⁺, which is mainly compensated by Na⁺/H⁺ exchange. By expanding our study to a series of Mn-based oxides, we reveal that the air-stability of P2-Na_xTmO₂ is highly related to their oxidation features in the first charge process and further propose a practical evaluating rule associated with redox couples for air-stable Na_xTmO₂ cathodes.

¹State Key Laboratory for Physical Chemistry of Solid Surfaces, and Department of Chemistry, College of Chemistry and Chemical Engineering, Xiamen University, 361005 Xiamen, People's Republic of China. ²School of Energy Research, Xiamen University, 361005 Xiamen, People's Republic of China. ³Department of NanoEngineering, University of California San Diego, La Jolla, CA 92093, USA. ⁴Department of Materials Science and Engineering, College of Materials, Xiamen University, Xiamen, 361005 Fujian, People's Republic of China. ⁵Departamento de Química Inorgánica e Ingeniería Química, Instituto Universitario de Investigación en Química Fina y Nanoquímica, Universidad de Córdoba, Campus de Rabanales, Edificio Marie Curie, E-14071 Córdoba, Spain. ⁶State Key Laboratory of Metal Matrix Composites, School of Materials Science and Engineering, Shanghai Jiao Tong University, 200240 Shanghai, P. R. China. ⁷School of Chemistry, Chemical Engineering and Life Science and State Key Laboratory of Advanced Technology for Materials Synthesis and Processing, Wuhan University of Technology, 430070 Wuhan, Hubei, People's Republic of China. ⁸4135 Belle Meade Circle, 28012 Belmont, North Carolina, USA. ⁹National High Magnetic Field Laboratory, 1800 E. Paul Dirac Drive, Tallahassee, FL 32310, USA. ✉email: liujp@whut.edu.cn; yyang@xmu.edu.cn

Practical application is always the ultimate goal for state-of-the-art technologies and devices, such as perovskite solar cells, thin-film transistors, and electrochemical batteries¹. Air-stability is undeniably one of the key issues that researchers should consider, because any air-instable compounds must be prepared, stored and assembled in dry or even inert atmospheres, leading to an increase in expense and can even jeopardize whether they are successfully commercialized.

Sodium ion batteries (SIBs) promise the potential for large-scale grid storage, due to the high abundance and wide distribution of Na sources as compared to their lithium counterparts^{2–4}. Among various sodium storage cathodes, layered sodium transition metal oxides (Na_xTmO_2) have gained significant attention owing to their great variety of compositions, ease of scalable preparation and high reversible specific capacity⁵. In the past forty years^{6,7}, the Na_xTmO_2 family has been greatly enriched not only thanks to the tremendous efforts toward superior cathodes with higher energy density and more stable structures^{8–10}, but has also benefited from the development of electrolytes and characterization techniques^{11–14}. Nonetheless, Na_xTmO_2 electrodes are still haunted by three major challenges, i.e. irreversible phase transitions during cycling, insufficient electrochemical performances and air/moisture instability^{5,15}. The undesired structural transformations in charge/discharge processes, such as P2-O2 in $\text{Na}_{0.67}\text{Ni}_{0.33}\text{Mn}_{0.67}\text{O}_2$ ^{16–20}, P2-P2' in $\text{Na}_{0.67}\text{MnO}_2$ ^{10,21–23} and O3-P3 in $\text{NaNi}_{0.5}\text{Mn}_{0.5}\text{O}_2$ ²⁴, can be suppressed or delayed by element substitution, thus resulting in improved cycling stability and rate capability. The contact between air-instable Na_xTmO_2 and moisture-air usually produces cracks²⁵, electrical insulation species²⁶, and hydration phases²⁷, which result in a shorter lifetime and poorer rate capability of the exposed layered oxides^{28–30}. Therefore, air-stability is considered an important factor to evaluate a qualified Na_xTmO_2 electrode^{31–33}.

Recently, Manthiram's group reported that O3- $\text{NaNi}_{0.7}\text{Mn}_{0.15}\text{Co}_{0.15}\text{O}_2$ reacts with H_2O and CO_2 , generating NaOH , Na_2CO_3 , $\text{Na}_2\text{CO}_3\cdot\text{H}_2\text{O}$ and NiO on the particle surfaces and leading to declined electrochemical performances²⁶. However, these degradation (Ni loss) reactions have not yet been extensively observed in Ni-poor/Ni-free Na_xTmO_2 materials, whether exposed to air or immersed in water^{34,35}. Unlike degradation, H_2O insertion is widely encountered in P2- Na_xTmO_2 electrodes and can be easily distinguished by X-ray diffraction (XRD), because the intercalation of H_2O expands the interlayer distance of the Na^+ layers from ~ 5 to ~ 7 Å and even up to ~ 9 Å^{36–38}. Kubota et al. proposed the Na^+/H^+ exchange mechanisms in O3-type NaMeO_2 oxides³⁹ and Rojo's group further identified the presence of H^+ in the Na^+ layers using a neutron powder diffraction technique³⁰. In addition, in the presence of H_2O , CO_2 was believed to get inserted

into the transition metal layers of P2- $\text{Na}_{2/3}\text{Fe}_{0.5}\text{Mn}_{0.5}\text{O}_2$ ²⁸. These works provide valuable insights into the structural evolutions of Na_xTmO_2 upon air-exposure. However, rational connections between these intertwined reactions, especially as to why and when the water molecules insert into the Na^+ layers, and which factor determines the extent of the structural transformation have not been thoroughly studied yet.

Fundamental understanding of structural/chemical evolutions in moisture is not only critical for the employment of Na_xTmO_2 as electrodes in both organic and aqueous SIBs, but also provides guidance to the fabrication and application of layered transition metal oxides in other battery systems, such as the favorable Ni-rich^{40–43} cathodes for lithium ion batteries. For layered sodium-based oxides, it is widely recognized that the air-instability in P2-type oxides is much more severe than that in O3-type Na_xMnO_2 ⁵. Herein, based on the P2- $\text{Na}_{0.67}\text{MnO}_2$ and P2- $\text{Na}_{0.67}\text{Ni}_{0.33}\text{Mn}_{0.67}\text{O}_2$ oxides, we unearth the underlying science that triggers the hydration of P2- Na_xTmO_2 , apply unique solid-state nuclear magnetic resonance techniques (ss-NMR) to provide solid evidence for H^+ insertion, analyze critical factors that influence the hydration, and outline the structural and chemical evolution mechanisms of P2- Na_xTmO_2 oxides upon air exposure. Importantly, the surface-sensitive time-of-flight secondary ion mass spectroscopy (TOF-SIMS) results reveal that the CO_2 cannot insert into the layered structure. Our results indicate that Na^+/H^+ exchange, rather than O_2 oxidation, dominates the compensation of extracted Na^+ and the hydration is closely related to the contents of remaining Na^+ ions in the structure. The critical sodium content n_c is therefore proposed to evaluate whether H_2O is able to intercalate into the sodium layers. In addition, the study of a series of P2- Na_xTmO_2 oxides indicates that the air-stability is closely associated with the voltage features of the charge process in the first cycle, and a practical principle related to the redox couple in the 1st cycle is thus proposed to evaluate the air-stability of Na_xTmO_2 . These new insights into the degradation mechanisms upon air-exposure will facilitate the development of practical layered Li/Na/K transition metal oxides.

Results

Features of hydration phases. To investigate the air-stable mechanisms, the structures and characterizations of hydration phases should be clarified first. The $\text{Na}_{0.67}\text{MnO}_2$ sample attained by solid-state reaction exhibits a typical P2 structure (space group: $P6_3/mmc$) with a layer spacing of ~ 5.5 Å (Fig. 1), according to the powder X-ray diffraction (XRD) patterns in Supplementary Fig. 1a. The commonly reported hydration impurity phase in the Na_xTmO_2 is birnessite^{27,30,37}, whose structure is very similar to that of P2- $\text{Na}_{0.67}\text{MnO}_2$, except the presence of extra water molecules in the sodium layers and a broader interlayer distance

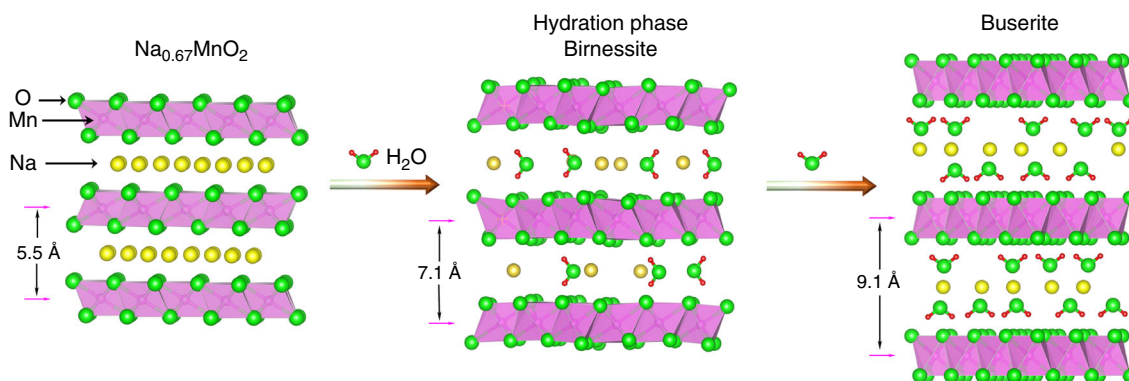


Fig. 1 Structural illustration of water insertion. Schematic illustration of P2- $\text{Na}_{0.67}\text{MnO}_2$, birnessite, and busierite phases.

of ~ 7.1 Å. With further H₂O insertion, the busierite phase with layer spacing of ~ 9.1 Å can be identified (Fig. 1 and Supplementary Fig. 1a). In addition to the difference in the interlayer spacing, the birnessite and busierite phases possess a different pattern of Na⁺ and H₂O arrangements in the sodium layers. For birnessite ($\{Na_{0.30} \cdot (H_2O)_{0.45}\}MnO_2$), according to the Rietveld refinement results⁴⁴ (Supplementary Table 1 and Fig. 1b) and the neutron powder diffraction patterns (NPD)⁴⁵, the O ion of inserted H₂O molecule locates at the same site of Na⁺; while for the highly hydrated busierite ($\{Na_{0.24} \cdot (H_2O)_{2.1}\}MnO_2$), the Na⁺ ions are sandwiched by the inserted H₂O molecules^{46,47}, as illustrated schematically in Fig. 1. Since busierite is seldom encountered in the moisture-exposed Na_xTmO₂, the hydration phase discussed below is referred to birnessite phase unless otherwise specified. It should be further pointed out that the Na⁺ content in hydrated Na_{0.67}TmO₂ sample is < 0.67 due to the Na⁺ loss upon air-exposure, as shown in the following sections. XRD, NPD and ²³Na magic-angle-spinning nuclear magnetic resonance spectroscopy (MAS NMR, Supplementary Figs. 1–3 and Note 1) are three powerful techniques to identify the hydration impurities (birnessite) in Na_xTmO₂ oxides, by characterizing the structural transitions, i.e. increased interlayer spacings. Fourier-transform infrared spectroscopy (FTIR) and ²³Na{¹H} rotational-echo double-resonance (REDOR)⁴⁸ can be used to detect the existence of water molecules and protons in the Na_xTmO₂ compounds, respectively (Supplementary Fig. 4 and Notes 1, and 2).

The structural transitions of the moisture-exposed P2-Na_{0.67}TmO₂. To investigate the structural changes of P2-Na_xTmO₂ during the air-exposure, Na_{0.67}MnO₂ and Na_{0.67}Ni_{0.33}Mn_{0.67}O₂ were selected as model compounds for air-unstable and air-stable electrodes, respectively²⁷, to be exposed in different atmospheres of dry CO₂, relative humidity (RH) 18% (without CO₂), RH 15% + CO₂ (with presence of CO₂), and RH 93% + CO₂ for 3 days (“Methods” part). As shown in the XRD patterns (Fig. 2a, b) and inductively coupled plasma-atomic emission spectrometry (ICP-AES) results (Supplementary Table 2), the targeted materials were successfully prepared. It can be observed that all XRD peaks of Na_{0.67}MnO₂ remain unchanged when placed in the dry CO₂ atmosphere (Fig. 2a), revealing that water is an inevitable component to destabilize Na_{0.67}TmO₂. At the atmospheres of RH 18% and RH 15% + CO₂, the hydration peaks (labeled with ‡) emerge and their intensities increase with the presence of CO₂. With further increase in the relative humidity (RH 93% + CO₂), all of the XRD peaks can be indexed to the hydration phase and NaHCO₃ (labeled with ∇), indicating that the Na_{0.67}MnO₂ is totally hydrated and partial Na⁺ diffuses out from the sodium layers. For Na_{0.67}Ni_{0.33}Mn_{0.67}O₂, no obvious hydration peaks can be identified in all of the exposed samples (Fig. 2b), suggesting Na_{0.67}Ni_{0.33}Mn_{0.67}O₂ is more stable than Na_{0.67}MnO₂ in moist atmospheres. To quantify the hydration extent of the exposed samples, Rietveld refinements on the XRD patterns were conducted with a two-phase model and the results are shown in Fig. 2c. The mass ratios of hydrated phases in the exposed Na_{0.67}MnO₂ samples are 0%, 42%, 58%, and 100% at the atmosphere of dry CO₂, RH 18%, RH 15% + CO₂, and RH 93% + CO₂, respectively, revealing that P2-Na_xTmO₂ components are more vulnerable to H₂O with both the existence of CO₂ and the increment of relative humidity.

Figure 2d–i depicts the morphological change of Na_{0.67}MnO₂ and Na_{0.67}Ni_{0.33}Mn_{0.67}O₂ powder after the exposure to the atmosphere of RH 93% + CO₂ for 3 days. Scanning electron microscopy (SEM) images in Fig. 2d, g show that the surface of as-prepared Na_{0.67}MnO₂ and Na_{0.67}Ni_{0.33}Mn_{0.67}O₂ particles are clean and smooth. After exposure, severe delamination damages and a massive of intragranular cracks can be observed in hydrated

Na_{0.67}MnO₂ sample (Fig. 2e), as a result of the significant volume expansion of $\sim 30\%$ during the hydration process. Besides structural changes, NaHCO₃ particles are found on the surface of hydrated Na_{0.67}MnO₂, as shown in the energy dispersive X-ray spectroscopy (EDS) elemental mapping results (Fig. 2f). Moreover, the crystals with very regular morphologies can be observed in the exposed-Na_{0.67}MnO₂ powder (Supplementary Fig. 5a, b), which should be unambiguously identified to NaHCO₃, according to the FTIR (Supplementary Fig. 4a) and EDS mapping results in Supplementary Fig. 5c. The formation of sodium salt is also observed in the air-exposed electrodes. As shown in Supplementary Fig. 6, sodium bicarbonate particles with nanoflakes morphology appear at the surface of the active materials. For exposed-Na_{0.67}Ni_{0.33}Mn_{0.67}O₂ sample, as shown in Fig. 2h, a rough surface is formed and there is no evidence of crack and layer glide, indicating that the morphological change of Na_{0.67}Ni_{0.33}Mn_{0.67}O₂ during exposure is more moderate than the Na_{0.67}MnO₂ sample (Fig. 2e). However, the EDS mapping results in Fig. 2i reveal that the NaHCO₃ particles are formed on the surface of exposed Na_{0.67}Ni_{0.33}Mn_{0.67}O₂, indicating the Na⁺ loss in Na_{0.67}Ni_{0.33}Mn_{0.67}O₂ compound during exposure. In summary, the above XRD, SEM and EDS results indicate that Na_{0.67}MnO₂ samples experience chemical transitions upon air-exposure, and Na_{0.67}Ni_{0.33}Mn_{0.67}O₂ changes as well.

Several influential factors especially relative humidity must be taken into consideration during the air-exposure experiments, soaking the samples in water is therefore a widely accepted testing procedure for confirming the stability of layered Na_xTmO₂ oxides³¹. Moreover, water-stability is an important metric of Na_xTmO₂ when applied as aqueous battery electrodes. Therefore, the structural evolutions of Na_{0.67}MnO₂ and Na_{0.67}Ni_{0.33}Mn_{0.67}O₂ samples in water have also been investigated. The results in Supplementary Note 3 and detailed analysis in Supplementary Note 3 suggest that the structural transformation mechanisms of P2-Na_xTmO₂ in water are similar to that in moist air.

The role of CO₂. The presence of CO₂ makes a big difference in the structural transformations of P2-Na_xTmO₂ upon moisture-exposure (Fig. 2c). To characterize the functionality of CO₂, we applied the TOF-SIMS to ascertain whether CO₂ intercalates into the bulk of the P2-Na_xTmO₂ during hydration^{5,26–28,30}. In order to eliminate the influence of the surficial sodium bicarbonate species (Fig. 2f and Supplementary Fig. 4), we adopted a scavenging process (see details in the Methods section). The FTIR spectra in Fig. 3a reveal that NaHCO₃ in the hydrated Na_{0.67}MnO₂ sample is successfully removed. TOF-SIMS depth profiles acquired on the scavenged powder show that the H₂O (OH⁻) and Mn ions (MnO⁻ and MnO₂⁻) appear at both surface and bulk of the powder (Fig. 3b), in good agreement with our refinement results (Supplementary Table 1). The signal intensity of C₂HO⁻ in the bulk (~ 165 a.u., Supplementary Fig. 9 and Note 4) is only 2.5 % compared to that of the prevailed OH⁻ (65k a.u.). Considering that the water content in hydrated Na_{0.67}MnO₂ is ~ 0.45 mol per chemical formula unit (Supplementary Table 1), it is therefore reasonable to conclude that the C atoms in the bulk of the hydrated samples are negligible. Furthermore, the cross-sectional TOF-SIMS chemical mapping images of the tested secondary particles (Fig. 3c) show that the intensity of C-related species (e.g. C₂HO⁻, NaC₂O₂⁻, C⁻) is much lower than OH⁻ and Mn-based ions and the remaining carbonate trace is mainly distributed on the surface rather than the bulk of the particles. This fact coincides well with the depth profile results in Fig. 3b and Supplementary Fig. 9. Therefore, the function of CO₂ is to increase the acidity at the particle’s surface

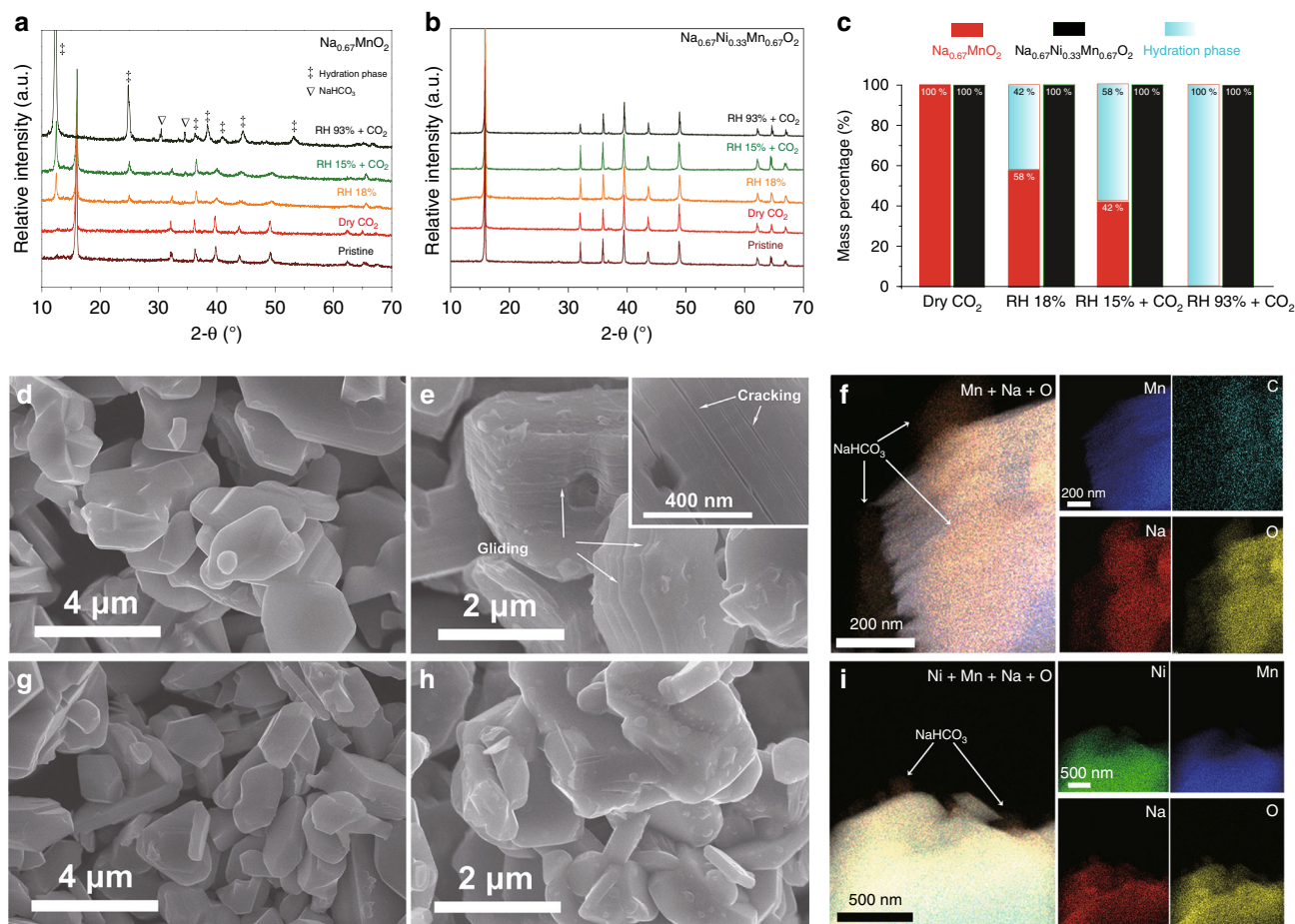


Fig. 2 The structural transitions of P2- $\text{Na}_{0.67}\text{TmO}_2$ upon air-exposure. The XRD patterns of **a** $\text{Na}_{0.67}\text{MnO}_2$ and **b** $\text{Na}_{0.67}\text{Ni}_{0.33}\text{Mn}_{0.67}\text{O}_2$ samples exposed in different atmosphere. **c** The refinement results of exposed $\text{Na}_{0.67}\text{MnO}_2$ and $\text{Na}_{0.67}\text{Ni}_{0.33}\text{Mn}_{0.67}\text{O}_2$ samples with a two-phase model. The SEM images of **d** pristine and **e** RH 93% + CO_2 exposed $\text{Na}_{0.67}\text{MnO}_2$ powder, **f** The EDS mapping results of exposed $\text{Na}_{0.67}\text{MnO}_2$, indicating that NaHCO_3 is formed on the particles' surface. The SEM images of **g** pristine and **h** RH 93% + CO_2 exposed $\text{Na}_{0.67}\text{Ni}_{0.33}\text{Mn}_{0.67}\text{O}_2$ powder. **i** The EDS mapping results of RH 93% + CO_2 exposed $\text{Na}_{0.67}\text{Ni}_{0.33}\text{Mn}_{0.67}\text{O}_2$ samples, NaHCO_3 particles are also observed on the surface of exposed $\text{Na}_{0.67}\text{Ni}_{0.33}\text{Mn}_{0.67}\text{O}_2$. The exposure time of the above samples are 3 days.

and accelerate the Na^+ loss rather than insert into the bulk of the Na_xTmO_2 phases.

The critical sodium contents (n_c) for hydration. Although $\text{Na}_{0.67}\text{Ni}_{0.33}\text{Mn}_{0.67}\text{O}_2$ has been reported to be one of the most air-stable P2- Na_xTmO_2 oxides, the chemical change is observed in the EDS mapping as demonstrated in Fig. 2i. Furthermore, as shown in Fig. 4a, with longer exposure time, the intensity of the NaHCO_3 diffraction peaks increases while the (002) diffraction peak shifts to lower 2-theta (Supplementary Fig. 10), suggesting the gradual extraction of Na^+ from $\text{Na}_{0.67}\text{Ni}_{0.33}\text{Mn}_{0.67}\text{O}_2$ during exposure. To validate the identification of NaHCO_3 , the pristine and exposed $\text{Na}_{0.67}\text{Ni}_{0.33}\text{Mn}_{0.67}\text{O}_2$ samples are further scrutinized by FTIR. As shown in Supplementary Fig. 11, the characteristic peaks located at $600\text{--}2000\text{ cm}^{-1}$ in the FTIR spectrum of the exposed $\text{Na}_{0.67}\text{Ni}_{0.33}\text{Mn}_{0.67}\text{O}_2$ in RH 93% + CO_2 fit well with that of NaHCO_3 . The absence of the O–H stretching signal between ~ 2500 and 3500 cm^{-1} suggests that no H_2O intercalates into the sodium layers of $\text{Na}_{0.67}\text{Ni}_{0.33}\text{Mn}_{0.67}\text{O}_2$, which is highly consistent with the XRD results. In addition, as shown in Fig. 4b and Supplementary Fig. 12, the ^{23}Na MAS NMR signal of $\text{Na}_{0.67}\text{Ni}_{0.33}\text{Mn}_{0.67}\text{O}_2$ shifts to the upper field by 47 ppm, corresponding to the expansion of c parameter (Supplementary

Fig. 10). It is worth noting that the intensity of $^{23}\text{Na}\{^1\text{H}\}$ REDOR signal for the exposed $\text{Na}_{0.67}\text{Ni}_{0.33}\text{Mn}_{0.67}\text{O}_2$ sample decreases with ^1H irradiation as a function of the spin-echo time, as compared to that without ^1H irradiation. This result confirms that H^+ ions are in close proximity to the sodium atoms in the structure of the exposed $\text{Na}_{0.67}\text{Ni}_{0.33}\text{Mn}_{0.67}\text{O}_2$ sample. Thus, it is more likely that the H ions replace those lost Na^+ , indicative of the Na^+/H^+ exchange mechanism. Moreover, given that the exposed electrodes usually exhibit improved open circuit potential²⁶, another charge compensation mechanism, i.e. the oxidation of transition metal ions by O_2 has been also proposed⁵. To validate which mechanism dominates the Na^+ loss process, X-ray absorption spectroscopy (XAS) was carried out. According to the previous results^{8,20,49}, during the first charge process of $\text{Na}_{0.67}\text{Ni}_{0.33}\text{Mn}_{0.67}\text{O}_2$ electrode within 2.0–4.4 V (vs. Na^+/Na), Mn^{4+} ions remain stable and the oxidation/reduction of Ni ions compensates the electrochemical extraction/insertion of Na^+ . As shown in Supplementary Fig. 13a, both position and shape of the Ni K-edge remain unchanged, indicating that the valence state of Ni ions in the exposed $\text{Na}_{0.67}\text{Ni}_{0.33}\text{Mn}_{0.67}\text{O}_2$ is nearly the same as in the pristine sample. The valence state of Mn ions in pristine and hydrated $\text{Na}_{0.67}\text{MnO}_2$ samples has been also investigated by XAS. The pre-edge peak and main edge of Mn K-edge XAS

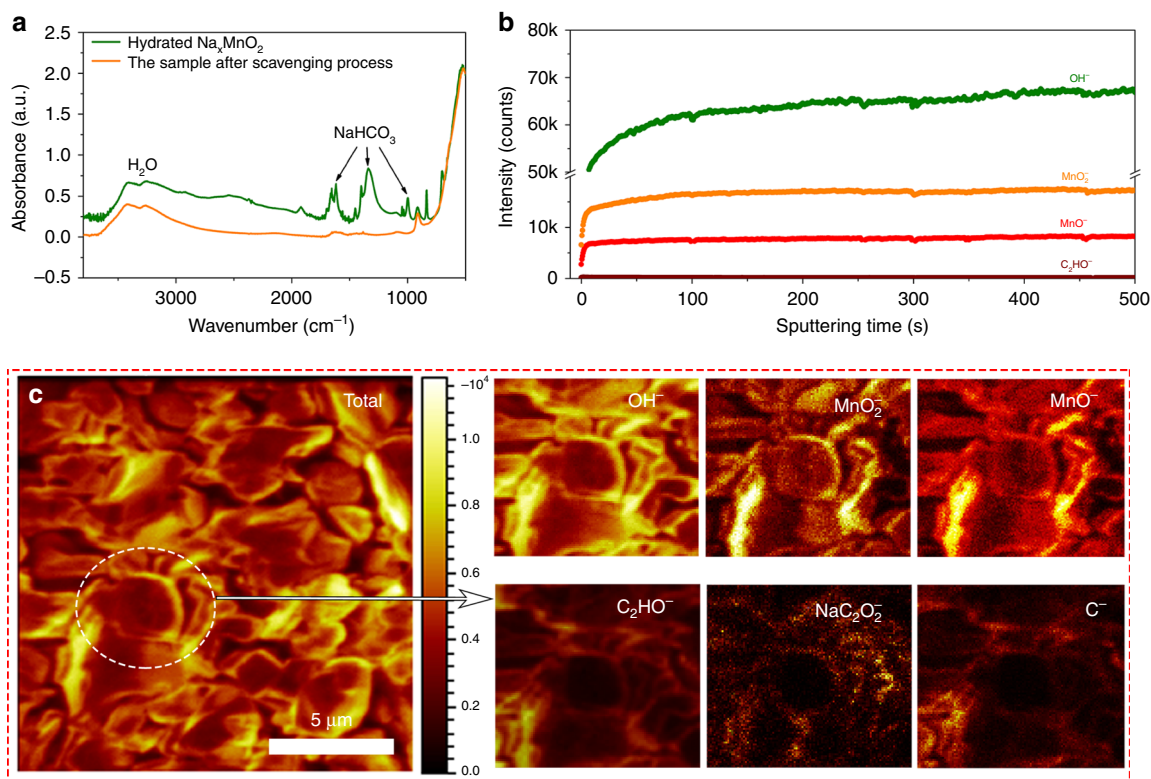


Fig. 3 TOF-SIMS results of the hydrated $\text{Na}_{0.67}\text{MnO}_2$ sample. **a** the comparison of FTIR spectra of the hydrated $\text{Na}_{0.67}\text{MnO}_2$ and hydrated $\text{Na}_{0.67}\text{MnO}_2$ after the scavenging process, indicating that after scavenging, most of the sodium (bi)carbonate impurities was removed. **b** TOP-SIMS spectra of OH^- , MnO^- , MnO_2^- , and C_2HO^- secondary ion fragments over 500 s Cs^+ sputtering along the depth profile of the sample after scavenging processes. **c** TOF-SIMS chemical mapping of the hydrated $\text{Na}_{0.67}\text{MnO}_2$ after the scavenging process, showing the distribution of OH^- , MnO_2^- , MnO^- , C_2HO^- , NaC_2O_2^- , and C^- secondary ions.

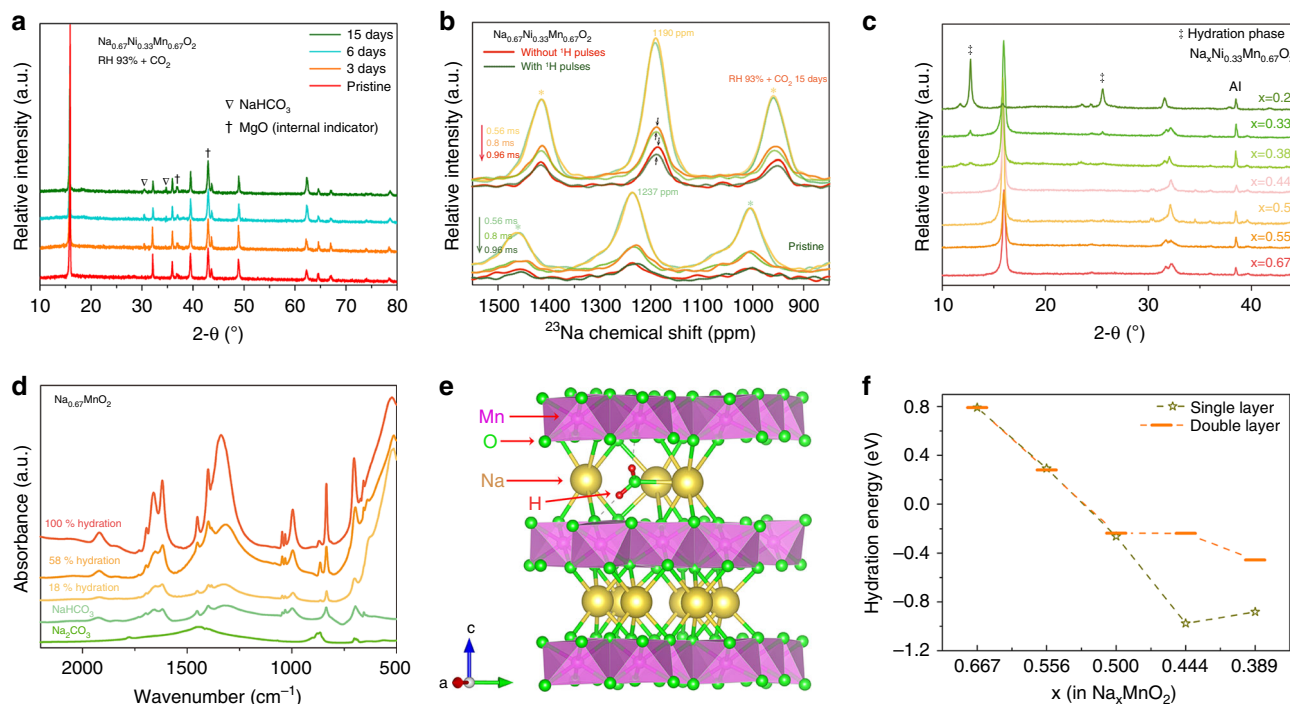


Fig. 4 The structural and chemical evolution mechanisms upon air-exposure. **a** The XRD evolutions of $\text{Na}_{0.67}\text{Ni}_{0.33}\text{Mn}_{0.67}\text{O}_2$ powder exposed at RH 93% + CO_2 atmosphere for different times (MgO was used as internal indicator). **b** $^{23}\text{Na}\{^1\text{H}\}$ REDOR-dephased ^{23}Na MAS NMR spectra (MAS rate: 25 kHz) and **c** The XRD patterns of exposed $\text{Na}_x\text{Ni}_{0.33}\text{Mn}_{0.67}\text{O}_2$ electrodes with various Na^+ content x . **d** The FTIR spectra of $\text{Na}_{0.67}\text{MnO}_2$ samples with various hydration degrees. **e** The structure model of single layer Na^+ loss structure for calculating hydration energies. **f** The calculated hydration energies for Na_xMnO_2 at various sodium contents x .

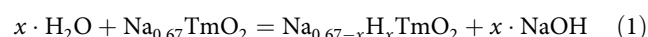
correspond to $1s \rightarrow 3d$ and $1s \rightarrow 4p$ transitions, respectively. However, the structural changes during hydration (Supplementary Fig. 13b) severely complicate the chemical shift of the main edge such that it becomes difficult to determine the valence state of Mn ions. Thus the pre-edge region could provide more reliable valent-state information⁵⁰. As can be seen from Supplementary Fig. 13b, the splitting and intensity of pre-edge peaks of Mn ions are similar for all of the pristine, partially hydrated and totally hydrated samples, indicating that the changes of the valence state of Mn ions are negligible during hydration. The XAS results suggest that Na^+/H^+ exchange might be the main reaction that compensates for the extracted Na^+ in the moisture-exposed Na_xTmO_2 . To confirm this conclusion, we stored the $\text{Na}_{0.67}\text{MnO}_2$ sample in three different atmospheres for 3 days, e.g. O_2 , RH 93% + CO_2 with the presence of O_2 , and RH 93% + CO_2 without O_2 . The XRD patterns in Fig. 2a and Supplementary Fig. 13c suggest that O_2 makes smaller difference than both CO_2 and water to the structural changes of Na_xTmO_2 .

To gain deeper insight into the structural/chemical transformation mechanisms of P2- Na_xTmO_2 materials upon air-exposure, a series of $\text{Na}_x\text{Ni}_{0.33}\text{Mn}_{0.67}\text{O}_2$ electrodes with different Na^+ contents were prepared by extracting Na^+ electrochemically, and then exposed at RH 93% + CO_2 atmosphere for 3 days. As shown in Fig. 4c, the hydration phase is absent at $\text{Na}_x\text{Ni}_{0.33}\text{Mn}_{2/3}\text{O}_2$ electrodes within sodium contents of $0.67 \leq x \leq 0.44$. In $x = 0.38$, the diffraction peaks of the hydration phase appear and its intensity increases with the further decrease of Na^+ contents. This result implies that hydration highly depend on the Na^+ contents. Specifically, if the sodium content x is lower than a critical sodium content n_c (0.38–0.44 for $\text{Na}_x\text{Ni}_{0.33}\text{Mn}_{2/3}\text{O}_2$ electrode), P2- Na_xTmO_2 materials are vulnerable for hydration and vice versa. The correlation between hydration degree and sodium contents x is also observed in Na_xMnO_2 compounds. As representatively shown in Fig. 4d, the intensity of NaHCO_3 absorption peaks are positively associated with the hydration degrees of $\text{Na}_{0.67}\text{MnO}_2$ sample.

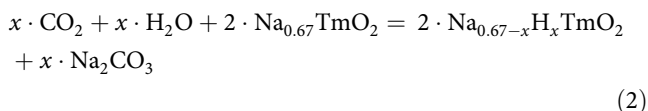
The density function theory (DFT) calculation was carried out to further understand the critical sodium content n_c . As shown in Fig. 4e and Supplementary Fig. 13d, two different sodium extraction models of single layer and double layer were considered, which correspond to the staging and random sodium extraction mechanisms, respectively¹⁵. The energy difference between P2- Na_xTmO_2 with and without water molecules is defined as hydration energy. DFT calculation results in Fig. 4f show that when $x > 0.52$, the hydration energy of Na_xMnO_2 is higher than 0 eV, suggesting that water molecules cannot get inserted into the material. When the sodium content is lower than 0.52, the hydration energy is lower than 0 eV, thus the hydrated structure is more stable than the un-hydrated structure. The foregoing energy analysis provides a chemical basis for understanding the sodium-content-dependent property in the hydration of Na_xMnO_2 samples. Due to the low formation energy, the layered $\text{Na}_{0.67}\text{TmO}_2$ oxides will lose Na^+ spontaneously once in contact with moist air. When the sodium contents are lower than n_c , there is a strong repulsion between adjacent oxide layers (TmO_2) of P2- Na_xTmO_2 oxides, and the insertion of H_2O could lower the energy of $\text{Na}_{0.67-x-z}\text{H}_x\text{TmO}_2$ (x and z correspond to the Na^+ loss that compensated by Na^+/H^+ exchange and O_2 oxidation, respectively) due to the shielding effect of the water molecule and the expansion of sodium layer spacings. The above results also proved and interpreted the fact that hydration takes place after the extraction of Na^+ during air-exposure.

Based on these results and analyses, the structural and chemical transformations of exposed P2- $\text{Na}_{0.67}\text{TmO}_2$ to different ambient atmospheres are summarized in Eqs. (1–4).

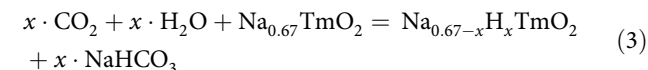
In the atmosphere without CO_2 :



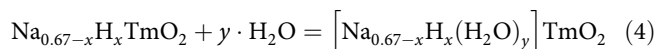
In the atmosphere with scarce CO_2 :



In the atmosphere with abundant CO_2 :



If the sodium content in the electrode is lower than n_c :



It should be emphasized that although Tm oxidation is not included in the proposed charge-compensation mechanisms due to lacking of direct spectroscopic evidences, there is still a high possibility that a minority of charge is compensated by the valence change of Tm ions. In the near future, more techniques, especially the state-of-the-art s-XAS characterizations are expected to obtain a deeper understanding of the charge-compensation mechanisms of Na^+ extraction in moisture-exposed Na_xTmO_2 .

The influence of structural changes on the electrochemical performances of P2- Na_xTmO_2 . In this section, we carefully investigate the influences of the above structural and chemical changes on the electrochemical performances of $\text{Na}_{0.67}\text{MnO}_2$ and $\text{Na}_{0.67}\text{Ni}_{0.33}\text{Mn}_{2/3}\text{O}_2$ electrodes. As shown in Fig. 5a, the pristine $\text{Na}_{0.67}\text{MnO}_2$ shows a high initial discharge capacity of 176 mAh g^{-1} at the current density of 12 mA g^{-1} within 2.0–4.4 V. After 50 cycles, 66 % of the initial capacity was retained, which coincides well with the previous results^{10,23}. For the hydrated $\text{Na}_{0.67}\text{MnO}_2$ electrode, the reversible capacity is negligible at the initial cycles. In the 9th cycle, although the discharge capacity increased to $\sim 150 \text{ mAh g}^{-1}$, abnormal electrochemistry, such as long charging plateaus, large voltage hysteresis and low coulombic efficiency are also observed. These deviant electrochemical performances indicate that the large amount of H_2O in the hydrated electrode has a pernicious influence on the organic-electrolyte based batteries.

The electrochemical performances of pristine $\text{Na}_{0.67}\text{Ni}_{0.33}\text{Mn}_{0.67}\text{O}_2$, $\text{Na}_{0.67}\text{Ni}_{0.33}\text{Mn}_{0.67}\text{O}_2$ exposed in RH 93% + CO_2 for 3 days (denoted as exposed- $\text{Na}_{0.67}\text{Ni}_{0.33}\text{Mn}_{0.67}\text{O}_2$), and $\text{Na}_{0.67}\text{Ni}_{0.33}\text{Mn}_{0.67}\text{O}_2$ immersed in water for 20 days (denoted as immersed- $\text{Na}_{0.67}\text{Ni}_{0.33}\text{Mn}_{0.67}\text{O}_2$) are presented in Fig. 5c–f. As shown in Fig. 5c, the pristine $\text{Na}_{0.67}\text{Ni}_{0.33}\text{Mn}_{0.67}\text{O}_2$, exposed- $\text{Na}_{0.67}\text{Ni}_{0.33}\text{Mn}_{0.67}\text{O}_2$, and immersed- $\text{Na}_{0.67}\text{Ni}_{0.33}\text{Mn}_{0.67}\text{O}_2$ samples have very similar initial charge-discharge curves, suggesting that their structure and redox center are nearly identical⁸. However, the initial charge capacities of the exposed- $\text{Na}_{0.67}\text{Ni}_{0.33}\text{Mn}_{0.67}\text{O}_2$ (70 mAh g^{-1}) and immersed- $\text{Na}_{0.67}\text{Ni}_{0.33}\text{Mn}_{0.67}\text{O}_2$ (77 mAh g^{-1}) are lower than that of the pristine $\text{Na}_{0.67}\text{Ni}_{0.33}\text{Mn}_{0.67}\text{O}_2$ (85 mAh g^{-1}), further confirming the loss of Na^+ ions during the exposure and immersing processes. Fig. 5d compares the cycling stability of the three electrodes. It can be observed that the exposed- $\text{Na}_{0.67}\text{Ni}_{0.33}\text{Mn}_{0.67}\text{O}_2$ exhibits much lower coulombic efficiency than the pristine $\text{Na}_{0.67}\text{Ni}_{0.33}\text{Mn}_{0.67}\text{O}_2$, due to the influence of the sodium bicarbonate on the surface of exposed- $\text{Na}_{0.67}\text{Ni}_{0.33}\text{Mn}_{0.67}\text{O}_2$ particles. At the voltage range of 2.0–4.0 V, the pristine $\text{Na}_{0.67}\text{Ni}_{0.33}\text{Mn}_{0.67}\text{O}_2$ material shows no evidence of capacity degradation after 100 cycles. In contrast, the immersed- $\text{Na}_{0.67}\text{Ni}_{0.33}\text{Mn}_{0.67}\text{O}_2$ and exposed- $\text{Na}_{0.67}\text{Ni}_{0.33}\text{Mn}_{0.67}\text{O}_2$ samples decay fast in capacity, and retain low discharge capacity of 56 and 53 mAh g^{-1} , corresponding to the capacity retention of 74% and 70%, respectively. To get more insight

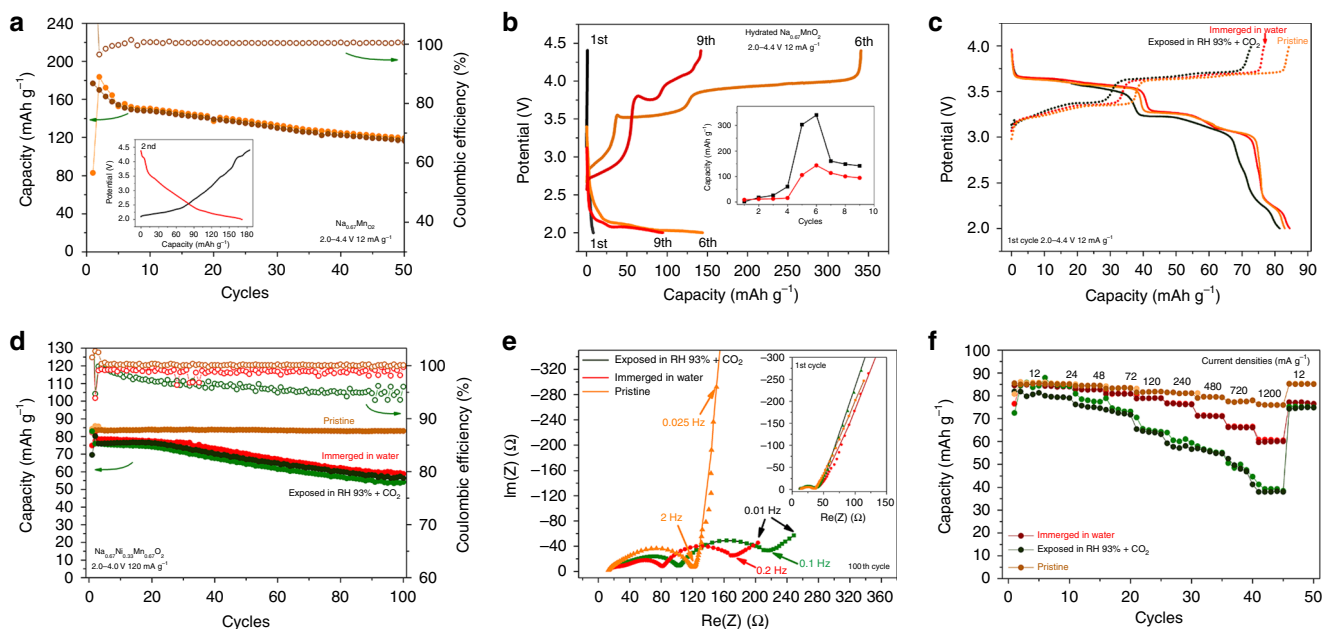


Fig. 5 Electrochemical performances of air-exposed $\text{Na}_{0.67}\text{MnO}_2$ and $\text{Na}_{0.67}\text{Ni}_{0.33}\text{Mn}_{0.67}\text{O}_2$. **a** The cycling performance of pristine $\text{Na}_{0.67}\text{MnO}_2$, the inset shows the charge-discharge curve at the 2nd cycle. **b** The charge-discharge curves and cycling stability of totally hydrated $\text{Na}_{0.67}\text{MnO}_2$ sample. **c–f** The electrochemical performances within the voltage range of 2.0–4.0 V of three $\text{Na}_{0.67}\text{Ni}_{0.33}\text{Mn}_{0.67}\text{O}_2$ samples (pristine $\text{Na}_{0.67}\text{Ni}_{0.33}\text{Mn}_{0.67}\text{O}_2$, $\text{Na}_{0.67}\text{Ni}_{0.33}\text{Mn}_{0.67}\text{O}_2$ samples immersed in water for 20 days and exposed in RH 93% + CO_2 for 3 days). **c** The initial charge-discharge curves at 12 mA g^{-1} . **d** The cycling stability of the three samples at 120 mA g^{-1} (after two formation cycles at 12 mA g^{-1}). **e** The comparison of the impedance responses at the 1st and 100th cycles with frequency varied from 100 kHz to 10 mHz. **f** The rate capability of three samples at the voltage range of 2.0–4.0 V.

into the degradation mechanisms, the electrochemical impedance spectra (EIS) have been employed to study the resistance changes. The interface and charge-transfer resistances were estimated based on the equivalent circuit in Supplementary Fig. 14 and summarized in Supplementary Table 3. In the first cycle, the electrode resistance of the three samples is quite similar (the inset in Fig. 5e). After 100 cycles, the rapid increase of the surface resistance (R_{SEI}) and charge transfer resistance (R_{CT}) for the exposed- $\text{Na}_{0.67}\text{Ni}_{0.33}\text{Mn}_{0.67}\text{O}_2$ and immersed- $\text{Na}_{0.67}\text{Ni}_{0.33}\text{Mn}_{0.67}\text{O}_2$ (Fig. 5e) samples indicates that the decomposition layer on the surface and the proton ions in the structure accelerate the depletion of the electrolyte thus blocking the diffusion of Na^+ ions. The comparison of rate capabilities shows a similar trend of cycling stability. As shown in Fig. 5f, the pristine $\text{Na}_{0.67}\text{Ni}_{0.33}\text{Mn}_{0.67}\text{O}_2$ electrode exhibits higher capacities than the immersed and exposed samples at all rates. The above electrochemical results demonstrate that exposure to moist air and immersion in water cause undesired structural changes and result in deteriorated electrochemical performances of P2- Na_xTmO_2 samples.

The structural transformation of hydrated phases upon calcination in air. We have concluded that the sodium extraction (mainly compensated by Na^+/H^+ exchange) and H_2O insertion are two continuous structural transition processes during the exposure of P2- Na_xTmO_2 samples, which usually impair their intrinsic electrochemical performances. The following questions need to be clarified: (i) whether or not these exposed samples can be recovered to their original structure and how, and (ii) what is the stoichiometry of hydrated phases (birnessite)? Therefore, in this section, the structural transitions of hydrated samples at the temperature range of 25–570 °C were investigated by in situ variable-temperature XRD technique. As shown in Fig. 6, five different stages can be observed in the in situ variable-temperature XRD pattern of the hydrated $\text{Na}_{0.67}\text{MnO}_2$. The

mass loss at stage *a* (25–130 °C) is ~15.1%, which includes decomposition of NaHCO_3 ⁵¹ and extraction of water. At this stage, the hydration structure is well maintained. From stage *a* to stage *b*, the hydrated phase is most probably transformed into a protonated phase (Supplementary Fig. 15 and Note 5) by two-phase reaction mechanisms at ~130 °C. The crystallinity of the $\text{Na}_{0.67-x-z}\text{MnO}_2$ phase at stage *c* (217–297 °C) is much lower than stage *b*, which might be resulted from the loss of protons. In addition, the sodium carbonate begins to decompose and results in the mass loss in stage *c*. With further increase in temperature, the crystallinity of $\text{Na}_{0.67-x-z}\text{MnO}_2$ increases, as shown in stage *d*. It should be pointed out that the decomposition temperature of Na_2CO_3 is lower than 800 °C due to the small sizes of the Na_2CO_3 particles (Fig. 2 and Supplementary Fig. 5) and the catalytic effect of transition metal oxides on reducing the energy requirement of Na_2CO_3 decomposition⁵². When the temperature is higher than 483 °C, the (100) and (103) peaks (at ~35° and ~43°, respectively) of the P2 phase emerge gradually, indicating the P2- $\text{Na}_{0.67}\text{MnO}_2$ phase gradually recovers at stage *e*. However, the mass loss of 0.45% during 130–217 °C corresponds to $x = 0.61$ in $\text{Na}_{0.67-x-z}\text{H}_x\text{MnO}_2$, exceeding the amount of lost Na^+ ions ($x + z \approx 0.39$, Supplementary Table 4), suggesting that the decomposition of Na_2CO_3 begins at stage *b* (130–217 °C). In conclusion, with the increase of temperature, the hydrated $\text{Na}_{0.67}\text{MnO}_2$ sample undergoes dehydration and NaHCO_3 decomposition (70–130 °C), deprotonation (130–217 °C), Na_2CO_3 decomposition (>130 °C) and the recrystallization of P2 phase (>483 °C) process. In our recent work²³, we demonstrate that $\text{Na}_{0.67}\text{Zn}_{0.1}\text{Mn}_{0.67}\text{O}_2$ is a promising Na-ion battery cathode with outstanding cycling stability and better air-stability than $\text{Na}_{0.67}\text{MnO}_2$. Therefore, we also performed the in situ variable-temperature XRD of totally hydrated $\text{Na}_{0.67}\text{Zn}_{0.1}\text{Mn}_{0.9}\text{O}_2$ powder. Obviously, the structural transformation of the hydrated $\text{Na}_{0.67}\text{Zn}_{0.1}\text{Mn}_{0.9}\text{O}_2$ in Supplementary Fig. 16 is different from that of the hydrated $\text{Na}_{0.67}\text{MnO}_2$. From the hydration phase

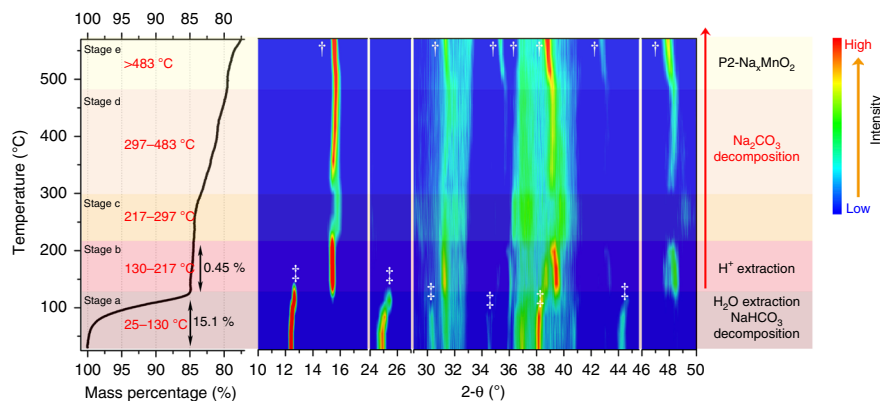
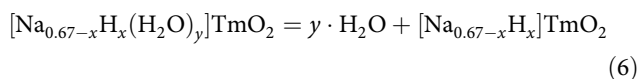
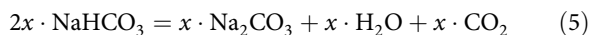


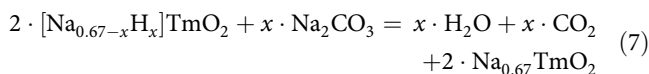
Fig. 6 Temperature-resolved in situ XRD of the totally hydrated $\text{Na}_{0.67}\text{MnO}_2$. The temperature ranges from 25 to 570 °C. The TGA curves are shown at the left. Hydrated and P2 phases are labeled with “ \ddagger ” and “ \dagger ”, respectively.

(stage *a*) to the protonated phase (stage *b*), the combined mechanism of two-phase and solid-solution reactions can be recognized. Moreover, the temperature range of deprotonation of the hydrated $\text{Na}_{0.67}\text{Zn}_{0.1}\text{Mn}_{0.9}\text{O}_2$ sample is elusive and the temperature of the recrystallization of P2-type $\text{Na}_{0.67}\text{Zn}_{0.1}\text{Mn}_{0.9}\text{O}_2$ phase (376 °C) is lower than that of $\text{Na}_{0.67}\text{MnO}_2$ (483 °C). The above results indicate that if the $\text{Na}_{0.67}\text{TMo}_2$ samples undergo sodium-loss and further hydration processes upon air-exposure, high-temperature annealing can be used to recover their original structures (the results of verification test are shown in Supplementary Fig. 17 and Note 6). Although the detailed structural transformation mechanisms during annealing are highly dependent on the stoichiometry of the exposed $\text{Na}_{0.67}\text{TMo}_2$, the general structural/chemical evolution processes are concluded in Eqs. (5–7) (Supplementary Note 7 and 8).

30–130 °C:



130–900 °C:



According to the structural/chemical evolution processes revealed by the above in situ XRD patterns, the chemical formulas of several hydrated $\text{Na}_{0.67}\text{TMo}_2$ materials, including $\text{Na}_{0.67}\text{MnO}_2$, $\text{Na}_{0.67}\text{Al}_{0.1}\text{Mn}_{0.9}\text{O}_2$, $\text{Na}_{0.67}\text{Cu}_{0.1}\text{Mn}_{0.9}\text{O}_2$, $\text{Na}_{0.67}\text{Zn}_{0.1}\text{Mn}_{0.9}\text{O}_2$, and $\text{Na}_{0.67}\text{Zn}_{0.2}\text{Mn}_{0.8}\text{O}_2$, are identified based on the TGA analysis (see detailed information in Supplementary Figs. 18 and 19, Table 4, Supplementary Eqs. (1–8), and Supplementary Note 8). ICP-AES analyses in Supplementary Table 4 are in good agreement with the chemical formulas of hydration phases. The results suggest that the contents of inserted H_2O vary greatly from ~ 0.1 to 0.45 depending on the stoichiometry of pristine materials.

The comprehensive structural/chemical evolution mechanisms upon air-exposure. Based on our analysis above, we summarize the structural and chemical transitions of the P2- $\text{Na}_{0.67}\text{TMo}_2$ components upon air exposure in Fig. 7a. At the initial stage, because of the low formation energy of layered $\text{Na}_{0.67}\text{TMo}_2$ oxides, the sodium ions are lost from the bulk and form amorphous $\text{Na}_2\text{CO}_3/\text{NaHCO}_3$ layer on the surface of particles or even $\text{Na}_2\text{CO}_3/\text{NaHCO}_3$ crystals with charge-compensation mechanism of Na^+/H^+ exchange. The formation energy increases with the

extraction of Na^+ ions and finally the P2- Na_xTMo_2 oxides are stable at the sodium content of 0.67-x-z in a specific environment. If the remaining sodium content 0.67-x-z is lower than the critical sodium content n_c , the water molecules go into the sodium layers and form the hydration phases. Considering the full decomposition of generated sodium salts and the recrystallization of the degraded structures, once the $\text{Na}_{0.67}\text{TMo}_2$ is protonated or hydrated, high-temperature calcination is needed to recover the hydrated forms back to the original structure. In addition to the above structural transitions, the outer layer of Na_xTMo_2 particles decomposes into transition-metal oxides/hydroxides when exposed to air or immersed in water. As shown in Supplementary Fig. 20, after exposing $\text{Na}_{0.67}\text{Cu}_{0.33}\text{Mn}_{0.67}\text{O}_2$ at RH 93% + CO_2 for 6 days, the Cu_2O and NaHCO_3 impurities can be observed in the XRD pattern, indicating that degradation is more or less an inevitable process at the surface of exposed $\text{Na}_{0.67}\text{TMo}_2$ compounds. Manthiram’s group also reported that the Ni-rich layered sodium oxide transforms into NiO and Na_2CO_3 in the surface²⁶. In brief, the structural and chemical transitions coexist, rather than a single protonation/Tm-oxidation, hydration, and degradation mechanism.

Evaluating the air-stability of Na_xTMo_2 electrodes. The choice and evaluation of air-stable Na_xTMo_2 electrodes have attracted enormous attention. It has been widely accepted that the Ni/Mn superlattice prevents the intercalation of H_2O since P2- $\text{Na}_{0.67}\text{Ni}_{0.33}\text{Mn}_{0.67}\text{O}_2$ was found to be resistant to hydration in moisture²⁷. However, our results demonstrate that $\text{Na}_{0.67}\text{Ni}_{0.33}\text{Mn}_{0.67}\text{O}_2$ is not as stable in moist air as it was expected, while other reported air-stable electrodes, such as $\text{Na}_{0.78}\text{Cu}_{0.27}\text{Zn}_{0.06}\text{Mn}_{0.67}\text{O}_2$ ³², $\text{Na}_{0.67}\text{Ni}_{0.22}\text{Cu}_{0.11}\text{Ti}_{0.11}\text{Mn}_{0.56}\text{O}_2$ ³⁵ and $\text{Na}_{0.79}\text{Cu}_{2/9}\text{Fe}_{1/9}\text{Mn}_{2/3}\text{O}_2$ ⁵³ do not have superlattice ordering in Tm layers. Therefore, the crucial factors, as well as the evaluation principles related to the air-stability of Na_xTMo_2 electrodes, have yet to be re-explored.

Therefore, we compared the air-stability of five layered oxides with different Mn valence-state and redox potential, e.g. $\text{Na}_{0.67}\text{MnO}_2$, $\text{Na}_{0.67}\text{Al}_{0.1}\text{Mn}_{0.9}\text{O}_2$, $\text{Na}_{0.67}\text{Zn}_{0.1}\text{Mn}_{0.9}\text{O}_2$, $\text{Na}_{0.67}\text{Zn}_{0.2}\text{Mn}_{0.8}\text{O}_2$ and $\text{Na}_{0.67}\text{Ni}_{0.33}\text{Mn}_{0.66}\text{O}_2$, at the atmosphere of dry CO_2 , RH 18%, RH 15% + CO_2 , and RH 93% + CO_2 . The XRD patterns and ICP-AES results of these pristine oxides are presented in Supplementary Fig. 21 and Table 5, respectively. In addition, the XRD patterns and the corresponding quantification of the hydration extents of the exposed samples are shown in Supplementary Fig. 22. According to the refinement results in Supplementary Fig. 22e, it is confirmed once again that more structural and chemical changes of $\text{Na}_{0.67}\text{TMo}_2$ occur with the increase of relative humidity and the presence of CO_2 . Moreover, it can be clearly observed

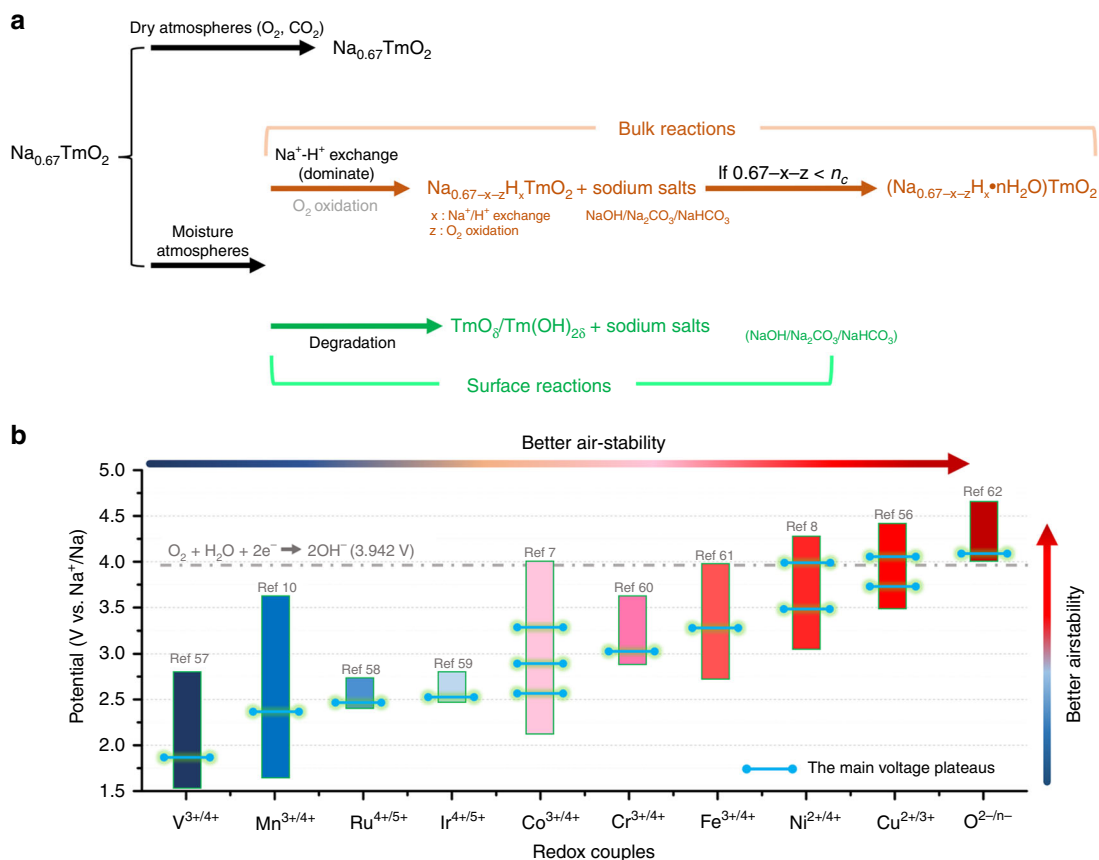


Fig. 7 Reaction pathways and evaluation rule. **a** Proposed reaction pathways for the moisture-exposed $Na_{0.67}TmO_2$ materials. **b** The comparison of the main redox couples in layered sodium transition metal oxides.

that the air-stability of these investigated layered oxides follows the order of $Na_{0.67}Ni^{2+}_{0.33}Mn^{4+}_{0.67}O_2 > Na_{0.67}Zn^{2+}_{0.2}Mn^{3.66+}_{0.8}O_2 > Na_{0.67}Zn^{2+}_{0.1}Mn^{3.47+}_{0.9}O_2 > Na_{0.67}Al^{3+}_{0.1}Mn^{3.37+}_{0.9}O_2 > Na_{0.67}Mn^{3.33+}O_2$, suggesting that the air-stability is closely related to the valence state of Mn ions or the redox potential of the initial charge process (Supplementary Fig. 23). To confirm this hypothesis, several electrodes were prepared and exposed to the atmosphere of RH 93% + CO_2 . As shown in Supplementary Fig. 24, although the valence state of Mn ions in $Na_{0.67}Co^{3+}_{0.67}Mn^{4+}_{0.33}O_2$, $Na_{0.67}Ni^{2+}_{0.17}Co^{3+}_{0.33}Mn^{4+}_{0.50}O_2$ and $Na_{0.67}Ni^{2+}_{0.17}Fe^{3+}_{0.33}Mn^{4+}_{0.50}O_2$ electrodes are Mn^{4+} , all of these samples are hydrated after three days' exposure in the atmosphere of RH 93% + CO_2 , indicating that the valence state of Mn ions is not the key parameter for the air-stability property. Therefore, $Na_{0.67}Li_{0.20}Mn_{0.80}O_2$ ⁵⁴, $Na_{0.67}Mg_{0.28}Mn_{0.72}O_2$ ⁵⁵ and $Na_{0.67}Cu_{0.33}Mn_{0.67}O_2$ ⁵⁶ samples that have high initial charging potential were prepared and exposed to the same atmosphere. As shown in Supplementary Fig. 20 and 25, after the exposure for 3 or 6 days, no hydration peaks can be recognized, indicating that the $Na_{0.67}TmO_2$ components with higher redox potential in the first cycles exhibit better air-stability. Generally, for a $Na_{0.67}TmO_2$ material with higher electrochemical redox potential (equilibrium potential), it is more difficult to extract Na^+ from the lattice chemically. Therefore, the potential of redox couples could be considered as one of the key principles to evaluate the air-stability of $Na_{0.67}TmO_2$ electrodes. Based on the above conclusion, we summarize the main redox couples in $P2-Na_xTmO_2$ electrodes (Fig. 7b), including $V^{3+/4+}$ ⁵⁷, $Mn^{3+/4+}$ ¹⁰, $Ru^{4+/5+}$ ⁵⁸, $Ir^{4+/5+}$ ⁵⁹, $Co^{3+/4+}$ ⁷, $Cr^{3+/4+}$ ⁶⁰, $Fe^{3+/4+}$ ⁶¹, $Ni^{2+/4+}$ ⁸, $Cu^{2+/3+}$ ⁵⁶, and $O^{2-/n-}$ ⁶². The result suggests that the electrodes with redox couples of $Ni^{2+/4+}$, $Cu^{2+/3+}$, and $O^{2-/n-}$ show much better

air-stability than that with the redox couples of $V^{3+/4+}$, $Mn^{3+/4+}$, $Co^{3+/4+}$, $Fe^{3+/4+}$, etc., which is in good agreement with the previous articles^{5,32,34,35,63}.

Besides chemical compositions, the crystallinity of $Na_{0.67}TmO_2$ also makes a great difference to their air-stability. Supplementary Fig. 26a,b show the weight loss and XRD evolutions during the preparation process of $Na_{0.67}MnO_2$, respectively. When the temperature increases to 480 °C, Na_2CO_3 begins to decompose and the β - MnO_2 (JCPDF: 72-1984) starts to transform into the layered $Na_{0.67}MnO_2$. The XRD peaks of β - MnO_2 disappear at ~540 °C and all of the Na_2CO_3 is decomposed at ~640 °C. We compared the air-stability of the $Na_{0.67}MnO_2$ samples at 640 °C, 900 °C, and the sample calcinated at 900 °C for 900 min, which exhibit increased crystallinity (Supplementary Fig. 26b). As shown in Supplementary Fig. 26c, after being exposed in RH 18% atmosphere for 3 days, the hydration degree follows the order of 640 °C > 900 °C > 900 °C 900 min samples, and clearly indicates that the samples with higher degree of crystallinity exhibit better air-stability.

Discussion

In summary, a comprehensive investigation of the structural and chemical transformations of $P2-Na_xTmO_2$ in different ambient atmospheres has been carried out. Using advanced technique characterizations and systematic investigation, we clarified and rationalized these intertwined reaction processes and their determining factors. For example, the critical roles of relative humidity and CO_2 in the air-stability of $P2-Na_{0.67}TmO_2$, the extraction of Na^+ ions from $Na_{0.67}Ni_{0.33}Mn_{0.67}O_2$ when exposed to moist air or emerged in water, the influence of

moisture-exposure on the electrochemical performances of Na_xTmO_2 , the precise quantification of water contents in hydrated phases, and the significance of crystallinity on the air-stability of Na_xTmO_2 , etc. Furthermore, based on the detailed mechanisms, including the Na extraction at the initial stage of moisture-exposure, the dominate Na^+/H^+ exchange charge-compensation mechanism, and the critical sodium content (n_c), we proposed a general and in-depth picture on the chemical/structural evolutions of $\text{P2-Na}_x\text{TmO}_2$ during moisture-exposure. In addition, by extending the study to a variety of layered sodium-based oxides ($\text{Na}_{0.67}\text{M}_x\text{Mn}_{1-x}\text{O}_2$, with $\text{M} = \text{Ni, Zn, Fe, Al, Co, Li, Mg, Cu, etc.}$) we have also demonstrated that the redox potential properties in the first charge process could be used as an empirical rule for evaluating the air-stability of Na_xTmO_2 electrodes. Our results provide significant new clues for the design, synthesis, storage, and application of layered sodium cathodes, as well as other alkali-metal transition metal oxides.

Methods

Preparation of layered materials. The pristine Na_xTmO_2 cathodes have been synthesized by high-temperature solid-state reactions^{12,23}. Stoichiometric amounts of raw materials, e.g. MnO_2 (99.95%, Aladdin), ZnO (99.99%, Aladdin), NiO (99.99%, Aladdin), Al_2O_3 (99.99%, Aladdin), TiO_2 (99.8%, Aladdin), CuO (99.9%, Aladdin), Li_2CO_3 (99.99%, Aladdin), and Na_2CO_3 (99.99%, Aladdin) were ball-milled with acetone solvent for 3.5 h at 500 rpm. Then dried at 120 °C overnight, pressed into pellets and heated at 900 °C for 15 h in air. After slowly cooled to 150 °C in the furnace, the pellets were transferred to an Ar-filled glove box immediately, ground and kept the final products in the Ar-filled glove box.

Hydration tests. The saturated salt solutions could produce stable relative humidity in a closed system at a certain temperature^{64,65}. To study the effect of different ambient atmospheres on the structural and chemical stability of Na_xTmO_2 , the prepared $\text{Na}_{0.67}\text{TmO}_2$ oxides are put in a centrifuge tube and then aged on an airtight container under four different storage conditions at the constant temperature of 40 °C. They are dry CO_2 , controlled humidity of RH 18% (without CO_2), RH 15% with CO_2 , and RH 93% with CO_2 . To maintain the ambience conditions of dry CO_2 , RH 15% with CO_2 and RH 93% with CO_2 , the dry silica gel, saturated aqueous LiCl and NaHCO_3 solutions are placed below the samples, respectively. After that, the containers are filled with CO_2 . The RH 18% (without CO_2) atmosphere was obtained by placing the saturated NaOH solution at the bottom of the container and then filled with dry O_2 . The accurate RH is determined by a hygrometer, whose accuracy is $\pm 1\%$. The elemental compositions of pristine and exposed samples were confirmed by inductively coupled plasma-atomic emission spectrometry (ICP-AES) analysis (IRIS Intrepid II XSP, Thermo Electron). Before ICP-AES and Time-of-flight secondary ion mass spectrometry (TOF-SIMS) testing, we applied a scavenging process to remove the $\text{Na}_2\text{CO}_3/\text{NaHCO}_3$ byproducts in the exposed samples. Specifically, the exposed samples were immersed and stirred in distilled water for 3 min, then centrifuged and dried at 80 °C overnight.

Characterizations. The X-ray diffraction (XRD) patterns were obtained on a Rigaku Ultima IV diffractometer by a Persee instrument with Cu K α radiation ($\lambda = 1.5406 \text{ \AA}$). The patterns were refined by the General Structure Analysis System (GSAS) software⁴⁴. The morphologies of samples were characterized by scanning electron microscopy (SEM, Hitachi S-4800). The EDS elemental mapping experiments were conducted using FEI Talos-F200s TEM instrument. The ^{23}Na ss-NMR experiments were acquired on a Bruker AVANCE III 400 MHz spectrometer using a double resonance 1.3 mm MAS probe spinning at frequencies of up to 55 kHz with a Hahn-echo pulse sequence (i.e. 90° pulse – τ – 180° pulse – τ , where τ is set to a multiple of rotor periods). The 90° pulse length of 1.2 μs and a recycle delay of 2 ms were used. The ^{23}Na shifts were referenced to 1 M NaCl aqueous solution (0 ppm). For ^1H , the 2.5 mm MAS probe was used spinning at 25 kHz to record the ^1H spectra with the rotor-synchronized Hahn Echo sequence and a cycle delay of 2 s and a 90° pulse length of 4 μs . No window functions were added and the chemical shift of ^1H was referenced against adamantane (1.87 ppm). By using 2.5 mm MAS probe with a MAS rate of 25 kHz, the rotational echo double resonance (REDOR) NMR sequence (i.e. the rotor-synchronized Hahn echo is applied on ^{23}Na , during τ periods the ^{23}Na - ^1H dipolar coupling is recovered by 180° ^1H pulses) is applied to confirm the presence of H^+ in the exposed materials. Geometry-independent information about the ^{23}Na - ^1H dipole couplings can be conveniently obtained from the plot of signal attenuation (1-scale) versus the dipolar evolution time (2tau). In all MAS NMR measurements, the variable temperature (VT) gas temperature was set to 315 K. The in situ XRD experiments were performed in air and on a BrukerD8 Discover diffractometer equipped with a Cu K α radiation. Infrared spectra were recorded on a Nicolet is50 FT-IR (Thermo

Fisher Scientific Inc., Madison, USA) spectrometer. X-ray absorption spectroscopy (XAS) data were acquired in the transmission mode at the BL14W1 beamline of the Shanghai synchrotron radiation facility (SSRF) at room temperature, and the incident beam was monochromatized by a Si (111) double-crystal monochromator. TOF-SIMS were performed on a TOF-SIMS5 spectrometer (ION TOF GmbH). The depth profiling and high-resolution mapping were conducted at the high current mode and burst alignment mode, respectively, with a pulsed Bi_1^+ ion beam (30 keV). The sputtering was conducted by a 500 eV Cs^+ ion beam with the area of $100 \mu\text{m} \times 100 \mu\text{m}$, and the analyzed areas for depth profiling and high-resolution mapping are typically $100 \mu\text{m} \times 100 \mu\text{m}$ and $50 \mu\text{m} \times 50 \mu\text{m}$ with the pixel of 128×128 .

Electrochemical tests. The electrodes are composed of 80 wt% of active materials, 10 wt% of polyvinylidene fluoride (PVDF) and 10 wt% acetylene carbon black. The mass loading of active materials is 2.5–3 mg cm^{-2} . The cleaned aluminum foil was used as current collector. The electrochemical performances were tested in 2025 coin cells which assembled in an Ar-filled glove box, using 1 M NaPF_6 in Propylene carbonate (PC, 98 vol%) and Fluoroethylene carbonate (FEC, 2 vol%) as the electrolyte, Whatman glass fiber filter as the separator, and sodium metal as the counter electrode. The galvanostatic charge-discharge processes were conducted on multichannel battery tester (Neware, CT-4008-5V10mA-164). The electrochemical impedance spectroscopy (EIS) was conducted by a four-channel multifunctional electrochemical workstation (Versa STAT MC, America), at the cell voltage of 4.0 V and with the frequency range of 100 kHz to 0.01 Hz.

DFT calculation. The DFT calculations were performed on VASP (Vienna ab initio Simulation Package)⁶⁶ and the exchange-correlation interactions of electron were described with spin-polarized generalized gradient approximation (GGA) and parameterized by PBE formula⁶⁷. The projector-augmented wave approach and GGA + U method were used to evaluate the electron-ion interactions and the localization of the d electrons of the TM ions, respectively^{68,69}. The U value of Mn set to 3.9 eV and the wave functions were expended by plane wave with a kinetic energy cut-off of 520 eV. The Monkhorst–Pack scheme⁷⁰ was used for the integration in the irreducible Brillouin zone with a k-point mesh resolution of $2\pi \times 0.025 \text{ \AA}^{-1}$. The lattice parameters and atomic coordinates were fully relaxed, and the final forces on all atoms were $< 0.01 \text{ eV \AA}^{-1}$. For the DFT calculations, a $3 \times 3 \times 1$ supercell, which contains 12 Na, 36 O, and 18 Mn has been adopted. Sodium contents of $x = 0.667, 0.556, 0.500, 0.444$ and 0.389 in Na_xMnO_2 correspond to 12, 10, 9, 8 and 7 Na ions in the supercell, and the number of different structures for each Na contents is $C_{12}^0, C_{12}^2, C_{12}^3, C_{12}^4$, and C_{12}^5 , respectively. Therefore, 1574 kinds of structures should be considered based on the enumeration method. Such computation load is however too heavy to be carried out and 9 of them have been calculated. Specifically, we considered two different sodium extraction models for the five different Na contents. The number of calculated structures for $x = 0.667, 0.556, 0.500, 0.444$ and 0.389 in Na_xMnO_2 are 1, 2, 2, 2, respectively, as shown in Fig. 4f (page 11 in the manuscript). Moreover, the residual Na sites were chosen randomly and then one water molecule was put into an empty Na site also randomly.

Data availability

All relevant data that support the findings of this study are presented in the manuscript and supplementary information file. Source data are available from the corresponding author on request.

Received: 18 January 2020; Accepted: 18 June 2020;

Published online: 15 July 2020

References

- Whittingham, M. S. Ultimate limits to intercalation reactions for lithium batteries. *Chem. Rev.* **114**, 11414–11443 (2014).
- Yabuuchi, N., Kubota, K., Dahbi, M. & Komaba, S. Research development on sodium-ion batteries. *Chem. Rev.* **114**, 11636–11682 (2014).
- Nayak, P. K., Yang, L., Brehm, W. & Adelhelm, P. From lithium-ion to sodium-ion batteries: advantages, challenges, and surprises. *Angew. Chem. Int. Ed.* **57**, 102–120 (2018).
- Vaalma, C., Buchholz, D., Weil, M. & Passerini, S. A cost and resource analysis of sodium-ion batteries. *Nat. Rev. Mater.* **3**, 18013 (2018).
- Wang, P.-F., You, Y., Yin, Y.-X. & Guo, Y.-G. Layered oxide cathodes for sodium-ion batteries: phase transition, air stability, and performance. *Adv. Energy Mater.* **8**, 1701912 (2018).
- Newman, G. H. & Klemann, L. P. Ambient temperature cycling of an Na-TiS₂ cell. *J. Electrochem. Soc.* **127**, 2097–2099 (1980).
- Delmas, C., Braconnier, J., Fouassier, C. & Hagenmuller, P. Electrochemical intercalation of sodium in Na_xCoO_2 bronzes. *Solid State Ion.* **3–4**, 165–169 (1981).

8. Zuo, W. et al. Structure-performance relationship of Zn²⁺ substitution in P2-Na_{0.66}Ni_{0.33}Mn_{0.67}O₂ with different Ni/Mn ratios for high-energy sodium-ion batteries. *ACS Appl. Energy Mater.* **2**, 4914–4924 (2019).
9. Yabuuchi, N. et al. P2-type Na_x[Fe_{1/2}Mn_{1/2}]O₂ made from earth-abundant elements for rechargeable Na batteries. *Nat. Mater.* **11**, 512–517 (2012).
10. Kumakura, S., Tahara, Y., Kubota, K., Chihara, K. & Komaba, S. Sodium and manganese stoichiometry of P2-type Na_{2/3}MnO₂. *Angew. Chem., Int. Ed.* **55**, 12760–12763 (2016).
11. Xu, K. Electrolytes and interphases in Li-ion batteries and beyond. *Chem. Rev.* **114**, 11503–11618 (2014).
12. Zuo, W. et al. Sodium storage behavior of Na_{0.66}Ni_{0.33-x}Zn_xMn_{0.67}O₂ (x = 0, 0.07 and 0.14) positive materials in diglyme-based electrolytes. *J. Power Sources* **400**, 317–324 (2018).
13. Fang, C. et al. Routes to high energy cathodes of sodium-ion batteries. *Adv. Energy Mater.* **6**, 1501727 (2016).
14. Shadik, Z. et al. Advanced characterization techniques for sodium-ion battery studies. *Adv. Energy Mater.* **8**, 1702588 (2018).
15. Clément, R. J., Bruce, P. G. & Grey, C. P. Review—manganese-based P2-type transition metal oxides as sodium-ion battery cathode materials. *J. Electrochem. Soc.* **162**, A2589–A2604 (2015).
16. Lu, Z. & Dahn, J. R. In situ X-ray diffraction study of P2-Na_{2/3}Ni_{1/3}Mn_{2/3}O₂. *J. Electrochem. Soc.* **148**, A1225 (2001).
17. Somerville, J. W. et al. Nature of the “Z”-phase in layered Na-ion battery cathodes. *Energy Environ. Sci.* **12**, 2223–2232 (2019).
18. Wang, Q. C. et al. Tuning P2-structured cathode material by Na-site Mg substitution for Na-ion batteries. *J. Am. Chem. Soc.* **141**, 840–848 (2018).
19. Wu, X. et al. P2-type Na_{0.66}Ni_{0.33-x}Zn_xMn_{0.67}O₂ as new high-voltage cathode materials for sodium-ion batteries. *J. Power Sources* **281**, 18–26 (2015).
20. Zhang, J., Wang, W., Wang, W., Wang, S. & Li, B. Comprehensive review of P2-type Na_{2/3}Ni_{1/3}Mn_{2/3}O₂, a potential cathode for practical application of Na-ion batteries. *ACS Appl. Mater. Interfaces* **11**, 22051–22066 (2019).
21. Clément, R. J. et al. Structurally stable Mg-doped P2-Na_{2/3}Mn_{1-y}Mg_yO₂ sodium-ion battery cathodes with high rate performance: insights from electrochemical, NMR and diffraction studies. *Energy Environ. Sci.* **9**, 3240–3251 (2016).
22. Liu, X. et al. P2-Na_{0.67}Al_xMn_{1-x}O₂: cost-effective, stable and high-rate sodium electrodes by suppressing phase transitions and enhancing Na⁺ mobility. *Angew. Chem., Int. Ed.* **58**, 18086–18095 (2019).
23. Zuo, W. et al. Highly-stable P2-Na_{0.67}MnO₂ electrode enabled by lattice tailoring and surface engineering. *Energy Storage Mater.* **26**, 503–512 (2020).
24. Zheng, S. et al. Exploring the working mechanism of Li⁺ in O3-type NaLi_{0.1}Ni_{0.35}Mn_{0.55}O₂ cathode materials for rechargeable Na-ion batteries. *J. Mater. Chem. A* **4**, 9054–9062 (2016).
25. Boyd, S., Dhall, R., LeBeau, James, M. & Augustyn, V. Charge storage mechanism and degradation of P2-type sodium transition metal oxides in aqueous electrolytes. *J. Mater. Chem. A* **6**, 22266–22276 (2018).
26. You, Y., Dolocan, A., Li, W. & Manthiram, A. Understanding the air-exposure degradation chemistry at a nanoscale of layered oxide cathodes for sodium-ion batteries. *Nano Lett.* **19**, 182–188 (2019).
27. Lu, Z. & Dahn, J. R. Intercalation of water in P2, T2 and O2 Structure A₂[Co_xNi_{1/3-x}Mn_{2/3}]O₂. *Chem. Mater.* **13**, 1252–1257 (2001).
28. Duffort, V., Talaie, E., Black, R. & Nazar, L. F. Uptake of CO₂ in layered P2-Na_{0.67}Mn_{0.5}Fe_{0.5}O₂: insertion of carbonate anions. *Chem. Mater.* **27**, 2515–2524 (2015).
29. Zhang, Y., Zhang, R. & Huang, Y. Air-stable Na_xTMO₂ cathodes for sodium storage. *Front. Chem.* **7**, 335 (2019).
30. Han, M. H. et al. Moisture exposed layered oxide electrodes as Na-ion battery cathodes. *J. Mater. Chem. A* **4**, 18963–18975 (2016).
31. Mu, L. et al. Prototype sodium-ion batteries using an air-stable and Co/Ni-free O3-layered metal oxide cathode. *Adv. Mater.* **27**, 6928–6933 (2015).
32. Yan, Z. et al. A hydrostable cathode material based on the layered P2@P3 composite that shows redox behavior for copper in high-rate and long-cycling sodium-ion batteries. *Angew. Chem., Int. Ed.* **58**, 1412–1416 (2019).
33. Guo, S., Li, Q., Liu, P., Chen, M. & Zhou, H. Environmentally stable interface of layered oxide cathodes for sodium-ion batteries. *Nat. Commun.* **8**, 135 (2017).
34. Chen, T. R. et al. Cu²⁺ dual-doped layer-tunnel hybrid Na_{0.6}Mn_{1-x}Cu_xO₂ as a cathode of sodium-ion battery with enhanced structure stability, electrochemical property, and air stability. *ACS Appl. Mater. Interfaces* **10**, 10147–10156 (2018).
35. Mu, L. et al. Water-processable P2-Na_{0.67}Ni_{0.22}Cu_{0.11}Mn_{0.56}Ti_{0.11}O₂ cathode material for sodium ion batteries. *J. Electrochem. Soc.* **166**, A251–A257 (2019).
36. Ching, S., Landrigan, J. A. & Jorgensen, M. L. Sol-gel synthesis of birnessite from KMnO₄ and simple sugars. *Chem. Mater.* **7**, 1604–1606 (1995).
37. Ching, S., Petrovay, D. J., Jorgensen, M. L. & Suib, S. L. Sol-gel synthesis of layered birnessite-type manganese oxides. *Inorg. Chem.* **36**, 883–890 (1997).
38. Bach, S., Pereira-Ramos, J. P., Baffier, N. & Messina, R. Birnessite manganese dioxide synthesized via a sol-gel process: a new rechargeable cathodic material for lithium batteries. *Electrochim. Acta* **36**, 1595–1603 (1991).
39. Kubota, K. & Komaba, S. Review—practical issues and future perspective for na-ion batteries. *J. Electrochem. Soc.* **162**, A2538–A2550 (2015).
40. Liu, H., Yang, Y. & Zhang, J. Reaction mechanism and kinetics of lithium ion battery cathode material LiNiO₂ with CO₂. *J. Power Sources* **173**, 556–561 (2007).
41. Pritzl, D. et al. Editors’ choice—washing of nickel-rich cathode materials for lithium-ion batteries: towards a mechanistic understanding. *J. Electrochem. Soc.* **166**, A4056–A4066 (2019).
42. Bianchini, M., Roca-Ayats, M., Hartmann, P., Brezesinski, T. & Janek, J. There and back again—the journey of LiNiO₂ as a cathode active material. *Angew. Chem., Int. Ed.* **58**, 10434–10458 (2019).
43. Jung, R. et al. Effect of ambient storage on the degradation of Ni-rich positive electrode materials (NMC811) for Li-ion batteries. *J. Electrochem. Soc.* **165**, A132–A141 (2018).
44. Toby, B. H. EXPGUI, a graphical user interface for GSAS. *J. Appl. Cryst.* **34**, 210–213 (2001).
45. Han, M. H. et al. High-performance P2-phase Na_{2/3}Mn_{0.8}Fe_{0.1}Ti_{0.1}O₂ cathode material for ambient-temperature sodium-ion batteries. *Chem. Mater.* **28**, 106–116 (2016).
46. Takada, K. et al. Superconductivity in two-dimensional CoO₂ layers. *Nature* **422**, 53–55 (2003).
47. Onda, A., Hara, S., Kajiyoshi, K. & Yanagisawa, K. Synthesis of manganese oxide octahedral molecular sieves containing cobalt, nickel, or magnesium, and the catalytic properties for hydration of acrylonitrile. *Appl. Catal., A* **321**, 71–78 (2007).
48. Gullion, T. & Schaefer, J. Detection of weak heteronuclear dipolar coupling by rotational-echo double-resonance nuclear magnetic resonance. *Adv. Magn. Optical Reson.* **13**, 57–83 (1989).
49. Wu, X. et al. Insights into the effects of zinc doping on structural phase transition of P2-type sodium nickel manganese oxide cathodes for high-energy sodium ion batteries. *ACS Appl. Mater. Interfaces* **8**, 22227–22237 (2016).
50. Rana, J. et al. Structural changes in Li₂MnO₃ cathode material for Li-ion batteries. *Adv. Energy Mater.* **4**, 1300998 (2014).
51. Ball, M. C., Snelling, C. M., Strachan, A. N. & Strachan, R. M. Thermal decomposition of solid sodium sesquicarbonate, Na₂CO₃·NaHCO₃·2H₂O. *J. Chem. Soc., Faraday Trans.* **88**, 631–636 (1992).
52. Dutcher, B. et al. Use of nanoporous FeOOH as a catalytic support for NaHCO₃ decomposition aimed at reduction of energy requirement of Na₂CO₃/NaHCO₃ based CO₂ separation technology. *J. Phys. Chem. C* **115**, 15532–15544 (2011).
53. Li, Y. et al. Air-stable copper-based P2-Na_{7/9}Cu_{2/9}Fe_{1/9}Mn_{2/3}O₂ as a new positive electrode material for sodium-ion batteries. *Adv. Sci.* **2**, 1500031 (2015).
54. Rong, X. et al. Structure-induced reversible anionic redox activity in Na layered oxide cathode. *Joule* **2**, 125–140 (2018).
55. Maitra, U. et al. Oxygen redox chemistry without excess alkali-metal ions in Na_{2/3}[Mg_{0.28}Mn_{0.72}]O₂. *Nat. Chem.* **10**, 288–295 (2018).
56. Kang, W. et al. Copper substituted P2-type Na_{0.67}Cu_xMn_{1-x}O₂: a stable high-power sodium-ion battery cathode. *J. Mater. Chem. A* **3**, 22846–22852 (2015).
57. Hamani, D., Ati, M., Tarascon, J.-M. & Rozier, P. Na_xVO₂ as possible electrode for Na-ion batteries. *Electrochem. Commun.* **13**, 938–941 (2011).
58. Mortemard de Boisse, B. et al. Intermediate honeycomb ordering to trigger oxygen redox chemistry in layered battery electrode. *Nat. Commun.* **7**, 11397 (2016).
59. Perez, A. J. et al. Strong oxygen participation in the redox governing the structural and electrochemical properties of Na-rich layered oxide Na₂IrO₃. *Chem. Mater.* **28**, 8278–8288 (2016).
60. Komaba, S., Takei, C., Nakayama, T., Ogata, A. & Yabuuchi, N. Electrochemical intercalation activity of layered NaCrO₂ vs. LiCrO₂. *Electrochem. Commun.* **12**, 355–358 (2010).
61. Yabuuchi, N., Yoshida, H. & Komaba, S. Crystal structures and electrode performance of alpha-NaFeO₂ for rechargeable sodium batteries. *Electrochemistry* **80**, 716–719 (2012).
62. Dai, K. et al. High reversibility of lattice oxygen redox quantified by direct bulk probes of both anionic and cationic redox reactions. *Joule* **3**, 518–541 (2019).
63. Zheng, L., Li, J. & Obrovac, M. N. Crystal structures and electrochemical performance of air-stable Na_{2/3}Ni_{1/3-x}Cu_xMn_{2/3}O₂ in sodium cells. *Chem. Mater.* **29**, 1623–1631 (2017).
64. Wang, Q. et al. Reaching the energy density limit of layered O3-NaNi_{0.5}Mn_{0.5}O₂ electrodes via dual Cu and Ti substitution. *Adv. Energy Mater.* **9**, 1901785 (2019).
65. Greenspan, L. Humidity fixed points of binary saturated aqueous solutions. *J. Res. Natl Bur. Stand. Sect. A: Phys. Chem.* **81A**, 89 (1977).

66. Kresse, G. & Furthmüller, J. Efficient iterative schemes for ab initio total-energy calculations using a plane-wave basis set. *Phys. Rev. B Condens Matter* **54**, 11169–11186 (1996).
67. Perdew, J. P., Burke, K. & Ernzerhof, M. Generalized gradient approximation made simple. *Phys. Rev. Lett.* **77**, 3865–3868 (1996).
68. Kresse, G. & Joubert, D. From ultrasoft pseudopotentials to the projector augmented-wave method. *Phys. Rev. B* **59**, 1758–1775 (1999).
69. Anisimov, V. I., Aryasetiawan, F. & Lichtenstein, A. First-principles calculations of the electronic structure and spectra of strongly correlated systems: the LDA+U method. *J. Phys.: Condens. Matter* **9**, 767 (1997).
70. Monkhorst, H. J. & Pack, J. D. Special points for Brillouin-zone integrations. *Phys. Rev. B* **13**, 5188–5192 (1976).

Acknowledgements

This work is financially supported by National Key Research and Development Program of China (grant no. 2018YFB0905400, 2016YFB0901502, 2016YFA0202602), National Natural Science Foundation of China (grant no. 21761132030, 21935009, 51972257). G.F. Ortiz acknowledges the Spanish Ministry of Science and Innovation (grant no. MAT2017-84002-C2-1-R and PRX18/00463). Dr. R. Fu thanks to the support from the National High Magnetic Field Laboratory, which is supported by NSF Cooperative Agreement NSF/DMR-1644779 and the State of Florida. Jimin Qiu acknowledges the grant from the National Science Fund for Fostering Talents in Basic Science (No. J1310024). We thank Dr. Jiaxin Ding in the Instrumental Analysis Center, Shanghai Jiao Tong University for her contribution in the TOF-SIMS analysis. We gratefully acknowledge the valuable time from beamline BL14W1 of the Shanghai Synchrotron Radiation Facility (SSRF).

Author contributions

W.Z., J.Liu, and Y.Y. conceived the project. Y.Y. supervised the project. W.Z., J.Q., J.Liu, M.W., Y.L., R.F., and Y.Y. designed the experiments. W.Z. and J.Q. performed the materials synthesis and electrochemical testing. W.Z., J.Q., X.L., H.H., H.L., C.L., and J.Li, performed the characterizations. F.R. completed the computational calculations. W.Z., J.Q., X.L., F.R., G.F.O., H.D., J.Liu, Y.L., R.F., and Y.Y., analyzed the data and proposed

the mechanisms. W.Z., J.Liu, R.F., and Y.Y., wrote the initial paper. All authors discussed the results and commented on the paper.

Competing interests

The authors declare no competing interests.

Additional information

Supplementary information is available for this paper at <https://doi.org/10.1038/s41467-020-17290-6>.

Correspondence and requests for materials should be addressed to J.L. or Y.Y.

Peer review information *Nature Communications* thanks the anonymous reviewers for their contribution to the peer review of this work.

Reprints and permission information is available at <http://www.nature.com/reprints>

Publisher's note Springer Nature remains neutral with regard to jurisdictional claims in published maps and institutional affiliations.



Open Access This article is licensed under a Creative Commons Attribution 4.0 International License, which permits use, sharing, adaptation, distribution and reproduction in any medium or format, as long as you give appropriate credit to the original author(s) and the source, provide a link to the Creative Commons license, and indicate if changes were made. The images or other third party material in this article are included in the article's Creative Commons license, unless indicated otherwise in a credit line to the material. If material is not included in the article's Creative Commons license and your intended use is not permitted by statutory regulation or exceeds the permitted use, you will need to obtain permission directly from the copyright holder. To view a copy of this license, visit <http://creativecommons.org/licenses/by/4.0/>.

© The Author(s) 2020